Sustainable Swine Manure Valorization: Gasification with High-Temperature Steam and CO_2 Blend

Sergey M. Frolov*, Viktor A. Smetanyuk, Ilias A. Sadykov, Anton S. Silantiev, Konstantin A. Avdeev, Fedor S. Frolov

Semenov Federal Research Center for Chemical Physics, 4, Kosygin Str., 119991 Moscow, Russia

** Corresponding author E-mail address: smfrol@chph.ras.ru*

Sergey M. Frolov: ORCID ID: https://orcid.org/0000-0002-5555-1876

Ilias A. Sadykov: ORCID ID: https://orcid.org/0000-0003-4688-3403

Fedor S. Frolov: ORCID ID: https://orcid.org/0000-0002-4237-9747

Viktor A. Smetanyuk: ORCID ID: https://orcid.org/0000-0003-4749-0142

Konstantin A. Avdeev: ORCID ID: https://orcid.org/0000-0001-7146-9672

Abstract: Experimental studies of sustainable, steam/CO_2-assisted allothermal gasification were conducted on raw wet swine manure (SM, 70% moisture) and partially dried SM (45% and 15% moisture). Tests were performed using a laboratory-scale flow-through gasifier equipped with cyclones for fly ash recovery. A pulsed detonation gun (PDG) fueled by a stoichiometric natural gas (NG)–oxygen mixture generated the high-temperature (~2000 K) gasifying agent (GA). The dry off-gas from the raw SM typically comprised 33–41 vol.% CO_2, 34–40 vol.% CO, 17–22 vol.% H_2, 2.5–6.0 vol.% CH_4, and 0–2.5 vol.% C_xH_y (with propane as the peak hydrocarbon below 0.1 vol.%), confirming tar-free gasification. Reducing SM moisture lowered the CO_2 yield to 26 vol.% while increasing CO, H_2, and CH_4 yields to 45, 25, and 5 vol.%, respectively. Measured off-gas temperatures and compositions closely matched thermodynamic calculations when accounting for heat losses. In the current laboratory setup, only 33% of the GA thermal energy is utilized for SM gasification, with 67% lost to the coolant and ambient environment. Under these conditions, gasifying 1 kg of dry SM using 1 kg of the stoichiometric NG–oxygen mixture yields 1.91 kg of combustible off-gas diluted with 26 vol.% CO_2. To achieve a self-sustaining process, a portion of this combustible off-gas can replace NG in the PDG. This approach was experimentally validated through off-gas detonability tests, where the stoichiometric off-gas–oxygen mixture achieved a detonation velocity of approximately 1800 m/s.

Keywords: swine manure valorization; allothermal gasification; gasifying agent; CO_2-assisted gasification; pulsed detonation

1. Introduction

One of the primary drivers behind rigid statutory frameworks for livestock by-products is the rapidly expanding volume of accumulated waste. The mismanagement of manure and droppings through storage on unequipped land sites frequently results in environmental contamination [1,2]. Within this category, swine manure (SM) represents the most critical environmental hazard due to significant concentrations of toxic components, namely ammonia, hydrogen sulfide, and mercaptans [3,4]. Therefore, viable technologies for the large-scale and high-volume processing of SM are needed as current solutions remain largely in the development phase.

A variety of modern methods are employed for SM processing, including biochemical routes such as accelerated composting [5,6], fertilizer production [7,8], and anaerobic digestion [9–11], as well as thermochemical technologies

like direct combustion [12–15], pyrolysis [16–19], hydrothermal conversion (liquefaction [20], carbonization [21], and supercritical water gasification [22,23]), and conventional gasification [24–27].

Currently, thermochemical methods are considered the most promising. In contrast to biochemical pathways characterized by prolonged processing times (weeks) and complex process control, thermochemical methods rely on relatively rapid thermolysis and conversion mechanisms. These processes effectively destroy pathogens [28], significantly reduce feedstock volume, and yield valuable outputs, whereas the recovered products include thermal energy, liquid biofuels, and syngas or biogas (mixtures of H_2, CO, light hydrocarbons, and CO_2) suitable for renewable power generation [29]. Additionally, the process yields a highly porous solid residue with an elevated concentration of nutrients like phosphorus, potassium, etc. [30], which can serve both as an agricultural fertilizer and a sorbent for heavy metals or organic pollutants [31]. However, the deployment of thermochemical methods for SM processing is typically hindered by its high moisture and ash content, necessitating additional separation and drying operations.

Direct combustion of SM in grate furnaces or fluidized bed reactors represents a practical approach for energy generation and greenhouse gas mitigation [32,33]. Nevertheless, the intensive flue gas cleaning required to remove hazardous emissions, including furans and dioxins, renders this method cost-prohibitive.

Pyrolysis of SM or its compost is highly energy-intensive, typically requiring the combustion of the SM feedstock itself or auxiliary organic matter. This process generally yields three product phases: biogas (10–20 wt.%), char (15–25 wt.%) [34], and pyrolysis oil (60–75 wt.%) [35,36]. Following water separation, the higher heating value (HHV) of the pyrolysis oil derived from raw SM and SM compost reaches 28.5 MJ/kg [37] and 31.2 MJ/kg [38], respectively. These values are significantly higher than those of wood-sawdust pyrolysis oil (23.9 MJ/kg) [38]. To upgrade this pyrolysis oil into commercial biofuel, multi-stage catalytic hydrotreating under high pressure is required [39]. However, the resulting biofuel exhibits high corrosivity, and converting it into syngas via steam reforming is severely restricted by catalyst poisoning and coking [40]. Concurrently, the char obtained from SM pyrolysis features high phosphorus, nitrogen, and sulfur contents, alongside low pH and electrical conductivity (EC) values [41].

Hydrothermal methods operate under extremely high pressures, which severely restricts their widespread industrial adoption [20–23]. For instance, hydrothermal liquefaction (depolymerization) of solid organic fractions in SM utilizes water at pressures of 10–25 MPa and temperatures of 550–640 K to yield a primary liquid biofuel with an HHV close to that of crude oil, alongside gas and solid by-products. Hydrothermal carbonization of SM occurs in an oxygen-deficient environment using a catalyst and water/steam at pressures up to 10 MPa and temperatures of 720–840 K; this pathway produces hydrogen-rich biogas and a liquid biofuel dense in phenols, nitrogen, and aromatics. Similarly, catalytic or non-catalytic gasification of SM with supercritical water (pressures > 22.1 MPa, temperatures > 650 K) – which benefits from the enhanced solubility of organic substances – yields high-quality syngas and an aqueous residual solution containing organic pollutants (phenols, substituted phenols, carbocyclic and N-heterocyclic compounds, benzene, and substituted benzenes).

For conventional SM gasification [24–27], a gasifying agent (GA) such as air, steam, or carbon dioxide is introduced at high temperatures (above 800 K) under atmospheric pressure. In an oxygen-deficient or completely oxygen-free environment, the organic constituents of SM are converted into syngas or off-gas. This gas can either be utilized for chemical synthesis (hydrogen, ammonia, methanol, etc.) or combusted in boilers, gas engines, and gas turbines. The gasification process exhibits higher energy efficiency than pyrolysis [42]. Although pyrolysis oil is more energy-dense than gasification products, the syngas obtained via gasification still maintains a substantial HHV of 15–20 MJ/Nm^3 [24,26].

Utilization of steam and carbon dioxide as GAs offers distinct advantages. First, because steam and CO_2 comprise only H/O and C/O atoms, the resulting syngas is free from inert gas dilution. Second, the high enthalpy of H_2O

and CO_2 significantly reduces the required volume of the GA. Third, operating in the absence of free oxygen prevents the formation of toxic compounds like furans and dioxins [43], thereby simplifying downstream purification. Fourth, steam gasification yields several times more hydrogen than air-blown gasification. Finally, CO_2 can be sourced directly from the flue gases of thermal power plants, providing a viable pathway for carbon capture and footprint reduction.

In general, steam/CO_2 gasification involves numerous heterogeneous and homogeneous endothermic and exothermic reactions between active radicals, atoms, and molecules, as well as electronically excited and ionized species in the case of plasma gasification. A highly simplified set of these overall reactions can be found, for instance, in [44]. According to recent literature, H_2O conversion proceeds via the highly endothermic primary steam-char gasification pathway, which is heavily coupled with gas-phase water-gas shift kinetics and steam reforming of hydrocarbons to maximize H_2 yields. Concurrently, the reaction pathways of CO_2 at high temperatures are dominated by the heterogeneous Boudouard reaction with char, alongside homogeneous pathways such as the reverse water-gas shift and dry reforming of methane and tars. In the literature, complex kinetic modeling is frequently substituted with equilibrium calculations, which generally predict qualitative trends rather than exact temperatures and species concentrations. Specifically, thermodynamic analyses of biomass steam/CO_2 gasification demonstrate that at temperatures around 900 K, carbon and oxygen are bound in CO_2, tar, and char, indicating low conversion rates. Above 1200 K, CO_2 reacts with the available carbon to yield CO, while oxygen preferentially reacts with carbon to form CO and CO_2 rather than with H_2 to form water. Finally, at temperatures exceeding 1500 K, tar and char are completely converted into syngas consisting primarily of H_2 and CO. Discrepancies between equilibrium predictions and experimental data are typically attributed to thermal losses, imperfect mixing, finite rates of heat and mass transfer, and chemical kinetic limitations.

In terms of potential capabilities, gasification is considered the most attractive thermochemical method for SM processing. However, conventional low-temperature technologies (up to 1200 K) suffer from major drawbacks – such as incomplete carbon conversion, high concentrations of condensable hydrocarbons (tars) in the off-gas, and the associated need for tar and char utilization – which limit their industrial scale-up [1,44]. To overcome these limitations, high-temperature gasification can be conducted at GA temperatures exceeding 1500 K. At these elevated thermal levels, the process yields clean, high-quality syngas alongside a stabilized, non-hazardous mineral slag.

The most high-temperature methods include allothermal electric-arc [45] and microwave [46] plasma gasification. In electric-arc reactors, the GA passes through an electric discharge plasma, reaching temperatures of ~10,000 K, and reacts with the waste at 1500–2000 K to convert it into syngas and slag, whereas in microwave reactors, the feedstock is heated via high-frequency (several GHz) electromagnetic radiation, driving gasification reactions within distributed "microplasma" nodes at temperatures up to ~5000 K. Despite these performance advantages, plasma gasification technologies face economic and operational barriers, namely intensive electricity consumption and the requirement for specialized, expensive refractory materials [44].

As an alternative to conventional allothermal processes, the pulsed detonation gun (PDG) gasification method [47] has proven effective for treating diverse organic wastes [48–51]. On the one hand, the PDG-generated steam/CO_2 mixture reaches temperatures over 2000 K, which is on par with electric-arc plasma gasification, and on the other hand, this approach circumvents the major drawbacks of plasma systems outlined above.

This study evaluates the application of this high-temperature technology to SM with varying moisture contents ($\alpha = 70\%, 45\%$, and 15%) to identify the critical criteria required for scaling the system into a viable and sustainable industrial process by examining syngas quality, the impact of biomass pre-drying, solid residue properties, thermal and mass balances, cold gas efficiency, as well as computational model validation, sustainability, and process scale-up.

2. Materials and Methods

2.1. Feedstock and gasifying agent

Raw wet SM served as the primary feedstock. Its solid fraction comprised multi-shaped particles with an average size of approximately 1 mm, while embedded bedding material ranged from 10 to 50 mm. The bulk density of the raw SM samples varied between 600 and 1250 kg/m³. Hot-surface drying characterization indicated that the moisture content of the raw wet SM spanned 67–74 wt.% (averaging 70 wt.%). The natural gas (NG) utilized as the fuel for the PDG consisted of 96.1 vol.% CH_4, 2.1 vol.% C_2H_6, 0.6 vol.% C_3H_8, 0.2 vol.% C_4H_{10}, and 1.0 vol.% N_2.

2.2. Experimental setup

Figure 1 shows the schematic diagram of the experimental setup primarily comprising a PDG, a vertical flow reactor, a gas cleaning system, and an off-gas burner. The PDG consists of a 600-mm-long cylindrical tube with an internal diameter (ID) of 50 mm, which is connected to a 900-mm-long splitter tube (40 mm ID). This assembly is equipped with a mixing and ignition device alongside a cooling jacket. To determine the detonation velocity within the PDG, two ionization probes (IPs) are positioned 250 mm apart. The PDG operates at a frequency of = 0.7–1 Hz injecting a high-velocity (~1 km/s), high-temperature (~2000 K) GA directly into the flow reactor (indicated by the dashed red arrow in Figure 1).

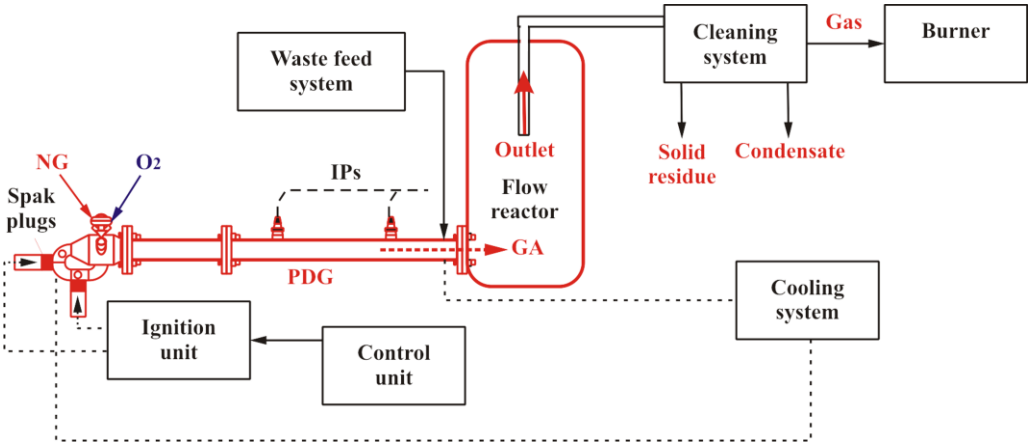

Fig. 1. Schematic of the experimental setup.

The flow reactor consists of a 50-L vessel fabricated from a standard gas cylinder shell. In contrast to the design in [51], this reactor features an upper hatch for feedstock loading and a bottom flange for tangential connection to the PDG via the splitter tube (Figure 2). The discharge line for gasification products (comprising off-gas, solid residues, and unreacted GA) exits through the upper reactor flange. These products flow continuously out of the reactor via a central 15-mm tube that extends 300 mm downward into the reactor cavity from the upper flange (indicated by the solid red arrow in Figure 1).

(*a*) (*b*)

Fig. 2. Flow reactor design: (a) schematic diagram highlighting the top hatch and splitter tube connection, and (b) photograph of the reactor showing the lower hatch configured for continuous feedstock supply above the PDG splitter tube.

Feedstock can be introduced into the system using two configurations: (1) batch feeding via the upper hatch (baseline operating mode), and (2) continuous feeding through the lower hatch. For continuous operation, a custom 3-L hydraulic piston feeder operating on a concrete-pump principle was developed. This mechanism ensures a stable feedstock delivery rate that is virtually independent of external operating factors.

The gasification process entails the entrainment of fine solid particles from the reactor bed, with their carbon conversion degrees varying across a wide range. To manage this, the downstream product purification system comprises a gas cooling unit sandwiched between two cyclones, culminating in an air-blown diffusion burner with a pilot flame for off-gas flaring and visual process monitoring. The product stream first passes through a 5-L dry cyclone for particulate separation, proceeds through the cooling system, and then enters a 2-L wet cyclone to capture the remaining condensate.

Mechanistically, the gasification process in the flow reactor shares key thermodynamic and transport features with combustion in a compression-ignition (Diesel) engine:

- Owing to external cooling, the reactor wall temperature remains substantially lower than that of the GA stream.
- Chemical transformations occur predominantly within the reactor core at elevated temperatures inside the feedstock–GA mixture.
- Due to the endothermic nature of the gasification reactions, the exiting off-gas temperature is significantly lower than the initial GA temperature.
- Each operational cycle involves the dilution of the fresh feedstock–GA charge with residual off-gas inside the reactor volume.

The specific diagnostic and measurement techniques employed in this study are detailed in Appendix A.

2.3. Experimental methodology

The feedstock was introduced into the reactor using either batch or continuous modes. In the batch configuration, a 0.5–1.0 kg charge of SM was loaded into the flow reactor prior to each test. Subsequently, the data acquisition, gas cooling, and PDG subsystems were activated, and the cyclic operation of the PDG was initiated at a designated frequency. The gasification process comprised two distinct stages: (i) moisture heating and evaporation, and (ii) thermochemical conversion of the dried biomass. The transition between these stages was monitored via the reactor temperature and the presence of off-gas combustion at the diffusion burner, the cessation of which marked the nominal completion of the gasification process. Although the recorded gas and wall temperatures in the upper reactor zone dropped to 250–350 °C by the end of the process, the primary gasification reactions occurred at localized, instantaneous GA temperatures exceeding ~2000 K. To investigate thermal effects, certain batch experiments involved preheating the empty reactor to a wall temperature of 170–300 °C. The batch tests evaluated SM with high (α ~70%), medium (α ~45%), and low (α ~15%) moisture contents.

Continuous feedstock delivery was executed via the hydraulic piston feeder at a volumetric flow rate of 0.5–3.3 mL/s, injecting into either an unheated reactor or one preheated to a wall temperature of 400 °C. Preheating enhanced the average internal temperature and improved the interaction uniformity between the feedstock particles and the supersonic GA jets, stabilizing the upper wall temperature at approximately 400 °C. To minimize the parasitic energy costs associated with moisture evaporation, the piston feeder mechanically dewatered the loose, wet feedstock prior

to injection. This compaction stage expressed excess water, reducing the feedstock density nearly threefold from 0.7 to 0.25 g/mL.

2.4. Methodology of thermodynamic calculations

In the thermodynamic model, the fuel (methane) and oxidizer (oxygen) are supplied to the PDG, premixed, and charged into the detonation tube. Upon ignition, a detonation wave propagates through the mixture, converting it into detonation products composed primarily of high-pressure, high-temperature steam and carbon dioxide. As these products enter the flow reactor, they expand to a pressure of 0.1 MPa, accompanied by a corresponding temperature drop. The dry SM introduced into the reactor undergoes thermal, mechanical, and chemical treatment by the dense (~2 kg/m^3) jet of detonation products, converting the biomass into off-gas. This off-gas continuously evacuates the reactor and is routed to downstream applications after cooling.

Thermodynamic calculations were performed using the methodology detailed in [52] under adiabatic conditions, neglecting heat losses to the environment. The GA is assumed to comprise the products of an ideal detonation of a stoichiometric methane–oxygen mixture, fully expanded to 0.1 MPa. The mixing between the feedstock and the GA is considered instantaneous, homogeneous, and complete, with graphite representing the condensed phase in the resulting gasification products.

3. Results

3.1. Measurements of feedstock properties

The average elemental composition of the dry SM, characterized using a PE 2400 Series II automatic CHNS/O analyzer (Perkin Elmer, USA), comprised 45.71 wt.% C, 37.72 wt.% O, 5.78 wt.% H, 1.64 wt.% N, 0.59 wt.% S, and 8.58 wt.% ash. The hydrogen content in the dry SM closely matches that of cellulose $(C_6H_{10}O_5)_n$, whereas the C and O concentrations deviate upward and downward, respectively, relative to cellulose (which contains 44.44% C, 49.34% O, and 6.22% H). Consistently, a comparison of the IR spectra of cellulose and the SM samples, recorded on an IRTracer-100 spectrometer (Shimadzu, Japan), revealed strong structural similarities. This indicates that the feedstock includes a cellulose-rich bedding material, such as wood sawdust. Beyond C, O, and H, the biomass contains minor nitrogenous and sulfurous compounds. Elemental X-ray fluorescence (XRF) analysis, performed on an ARL PERFORM'X spectrometer (Thermo Fisher Scientific Inc., USA; X-ray tube power 2500 W), demonstrated that the mass fraction of elements with an atomic mass greater than 11 is 6.8%. The inorganic matrix is primarily composed of Si, Ca, P, Mg, K, S, Na, Cl, Al, and Fe compounds. Finally, bomb calorimetry using an ABK-1V system (Russia) quantified the higher and lower heating values of the dried SM at $Q_{\mathrm{H,SM}}$ = 16.5 MJ/kg and $Q_{\mathrm{L,SM}}$ = 14.6 MJ/kg, respectively (see Appendix B).

3.2. Calculated chemical composition of gasification agent

The GA was generated via the pulsed detonation of a stoichiometric NG–oxygen mixture with a fuel-to-oxidizer equivalence ratio of $\Phi \approx 1.0$. Given that methane is the predominant component of NG, the fuel was modeled as pure methane in the thermodynamic simulations. The computed Chapman–Jouguet (CJ) detonation velocity for the stoichiometric methane–oxygen mixture reached 2380 m/s (Mach number $M_{\mathrm{CJ}} = 6.74$). In the CJ state, the temperature, pressure, and density of the detonation products were 3700 K, 2.94 MPa, and 2 kg/m³, respectively. Upon expansion to the baseline pressure ($P_0 = 0.1$ MPa), the temperature of the detonation products was 2853 K (2580 °C). These thermodynamic equilibrium calculations were executed using the SDToolbox [53] and Cantera [54] software

packages. When expanded to $P_0 = 0.1$ MPa and cooled to a characteristic thermal state of 2000 K, the evaluated composition of the detonation products comprised 65 vol.% H_2O, 32 vol.% CO_2, 2 vol.% CO, and 1 vol.% H_2. Thermodynamic modeling confirmed that this chemical composition remained frozen upon further cooling to lower temperatures.

3.3. Calculated chemical composition of gasification products

Thermodynamic simulations indicate that gasifying 1 kg of dry SM requires 0.3 kg of GA, establishing an optimal theoretical SM/GA mass ratio of $\Omega_t \approx 3.3$. At $\Omega_t > 3.3$ and gasification temperatures exceeding 1200 K, the solid carbon (graphite) yield escalates up to 11 vol.%. This condensed-phase formation diminishes the volume fractions of the primary off-gas components (H_2 and CO), consequently reducing the total mass of off-gas generated per kilogram of SM. Conversely, at $\Omega_t < 3.3$, the volumetric fractions of steam and carbon dioxide in the product stream increase, which lowers the mass of dry off-gas and degrades the off-gas heating value due to the elevated CO_2 concentration. The calculated thermodynamic equilibrium compositions of the dry off-gas comprise 57 vol.% CO, 40 vol.% H_2, and 3 vol.% N_2 at temperatures above 1500 K. At a lower thermal state of 1000 K, the predicted profile shifts to 10 vol.% CO_2, 45 vol.% CO, 41 vol.% H_2, and 4 vol.% N_2, where nitrogen originates exclusively from the SM matrix.

3.4. Measurement examples

Figures 3a and 3b illustrate representative transient profiles of the gas T_G and reactor wall T_W temperatures across two distinct experiments utilizing a 1-kg batch of raw SM (70% moisture) loaded via the upper hatch. In both trials, the PDG was activated at $t = 0$. The thermochemical conversion of SM is characterized by two sequential stages: moisture heating/evaporation and dry biomass gasification. The initial drying stage corresponds to the time interval τ_1, where T_G establishes a distinct thermal plateau at 100 °C. The subsequent gasification stage is defined by the time interval τ_2, finishing when the diffusion burner flame is quenched. In the baseline run (Figure 3a), these time intervals were recorded as $\tau_1 \approx 380$ s and $\tau_2 \approx 450$ s, yielding a total process duration of $\tau_\Sigma \approx 830$ s. Upon completion, T_G remained 30–40 °C higher than T_W. Figure 3b details the corresponding real-time evolution of the off-gas composition (left scale). The response time required for the gas analyzer to stabilize varies by chemical species and is governed by sensor kinetics, the scrubbing media, and process homogeneity, with a minimum stabilization threshold of ~300 s. To account for these transient lags, replicate tests were performed to validate reproducibility. For the trial shown in Figure 3b, the drying and gasification stages lasted approximately 240 s and 600 s, respectively ($\tau_\Sigma \approx 840$ s). The final dry off-gas comprised 32 vol.% CO_2, 40 vol.% CO, 21 vol.% H_2, 5 vol.% CH_4, and 2 vol.% C_xH_y (with 0 vol.% O_2), representing a total combustible fraction of 68 vol.%. Notably, the CO_2 concentration exhibited a pronounced peak during the first stage. This could be attributed to the initial influx of CO_2 from the GA stream prior to its partial consumption via endothermic gasification reactions.

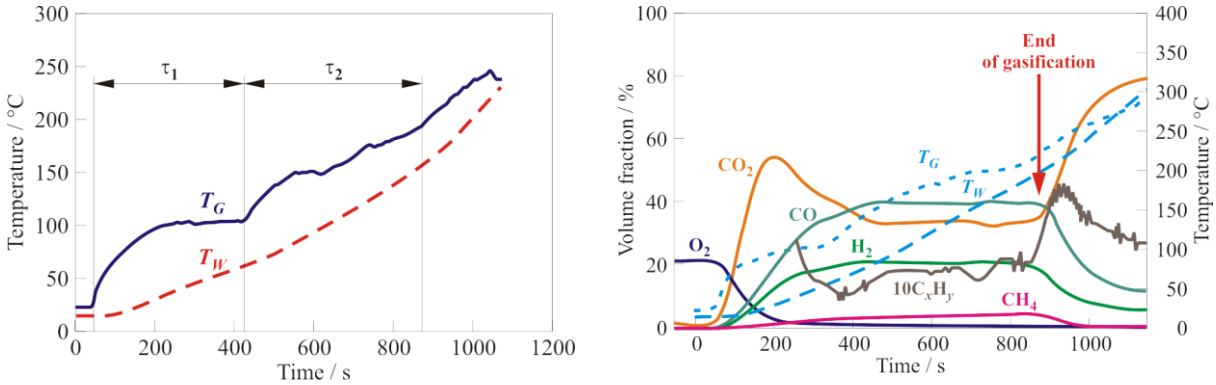

(a) (b)

Fig. 3. Representative transient profiles of gas temperature (T_G) and reactor wall temperature (T_W) at the top of the flow reactor (a) alongside the real-time dry off-gas composition (b) for two independent batch gasification experiments utilizing 1 kg of raw SM (70% moisture).

3.5. Measured composition of gasification products

The parameters and outcomes of 17 representative experiments conducted on SM are compiled in Table C1 in Appendix C (designated as runs #1 to #17). Gasification of the raw wet feedstock (α =70%) typically yielded a dry off-gas composed of 33–41 vol.% CO_2, 34–40 vol.% CO, 17–22 vol.% H_2, 2.5–4.0 vol.% CH_4, and 0–2.5 vol.% C_xH_y (Figure 4). Minimizing the CO_2 concentration directly correlated with an elevation in CO and H_2 fractions, whereas the hydrocarbon outputs remained largely invariant. For the pre-dried SM trials (α =15%), the CO_2 content dropped to 26–32 vol.%, while the peak concentrations of CO, H_2, and CH_4 advanced to 45, 25, and 4.5 vol.%, respectively, pushing the total combustible fraction up to 74 vol.%. The lower heating value (LHV) of the effluent gas ranged between 7 and 12 MJ/kg. These values can be obviously further enhanced by promoting the conversion of the GA-derived CO_2 within the reactor. Parametric analysis indicated that under identical feedstock mass and moisture constraints, increasing the PDG pulse frequency accelerated the transformation rate, thereby shortening the total processing time (as demonstrated by comparing runs #2, #3, and #8 with run #4). Conversely, increments in either initial moisture content (runs #16 vs. #17) or batch mass (runs #10 vs. #17) induced a clear reduction in the peak reactor wall temperature. These findings align with fundamental thermodynamic and heat transfer principles. The obtained dataset establishes the isolated impacts of key operational boundaries, like feeding configurations and initial wall temperatures, on the resulting off-gas composition, which are examined in the subsequent subsections.

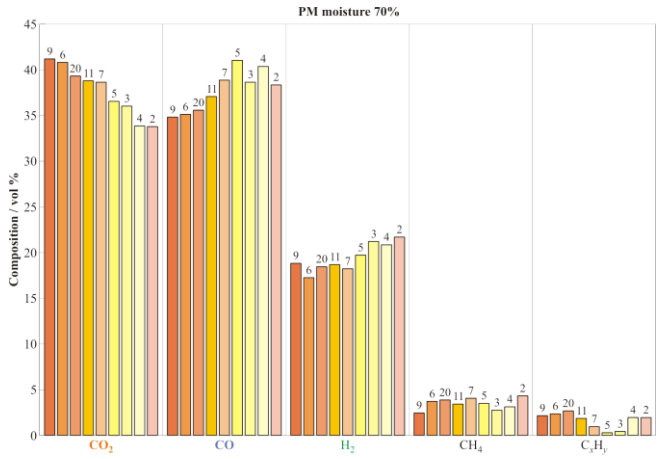

Fig. 4. Dry off-gas compositions obtained from the gasification of wet SM (70% moisture content) under various operating conditions with batch feedstock loading. The integers above the bars correspond to the run numbers listed in Table C1.

3.6. Clarified chemical composition of the off-gas

In runs #8, #9, #10, and #11, gas sampling for chromatographic analysis via a Chromatec-Crystal 2000 gas chromatograph was conducted in parallel with real-time off-gas characterization using the MRU VARIO Plus flow-through analyzer. Table 1 compares the volumetric fractions of the gas components obtained by the flow-through analyzer against those from the gas chromatograph (indicated by asterisks, *). The chromatographic samples in runs #8 and #9 were collected downstream of the bubbler unit, whereas in runs #10 and #11, the sampling point was located upstream of the bubbler. Comparative analysis demonstrated that the bubbling process had a negligible effect on the final off-gas composition.

Table 1. Comparison of dry off-gas compositions measured via the flow-through gas analyzer and gas chromatograph (indicated by asterisks, *) across selected gasification experiments.

Exp.#	CO_2 vol.%	CO vol.%	H_2 vol.%	CH_4 vol.%	C_xH_y vol.%	N_2 vol.%	C_2H_4 vol.%	C_2H_6 vol.%	C_3H_8 vol.%
8	41.3	34.7	18.7	2.5	2.2	-	-	-	-
8*	40.5	31.6	23.3	1.4	-	1.7	0.52	0.86	0.03
9	32.4	41.4	20	3.6	2.5	-	-	-	-
9*	28.3	39.5	26.1	1.9	-	2.0	0.84	1.34	0.05
10	38.7	37	18.7	3.5	1.9	-	-	-	-
10*	37.8	33.2	24.1	1.8	-	0.97	0.76	1.08	0.07
11	34.7	39.3	19.4	4	2.5	-	-	-	-
11*	34.5	35.6	24.4	2.1	-	0.79	1.03	1.47	0.1

A comparison of the instrument outputs indicates that the volumetric fractions of CO and H_2 determined via gas chromatography deviate from the flow-through analyzer readings by an average of –3% (abs.) for CO and +5% (abs.) for H_2. Unlike the flow-through analyzer, which quantifies only methane and logs all other hydrocarbons (C_xH_y) as inert N_2, the gas chromatograph provides a breakdown of the C_xH_y fraction. Propane was identified as the peak registered hydrocarbon, with a concentration below 0.1 vol.%. Beyond propane, the effluent off-gas contains trace amounts of ethylene and ethane so that the cumulative fraction of all detected hydrocarbons, including methane, remains below 5 vol.%. Consequently, the dry off-gas is free of hydrocarbons heavier than propane, confirming the absence of condensable organic fractions and tars.

3.7. Effect of the feedstock feeding method and the initial temperature of reactor on the dry off-gas composition

As an alternative to the baseline batch configuration, a hydraulic piston feeder was implemented to achieve a controllable, constant feedstock delivery rate into the flow reactor cavity. This gradual feeding approach was expected to enhance the mixing between the biomass and the GA, thereby accelerating carbon conversion efficiency, maximizing CO and H_2 outputs, and suppressing CO_2 formation. However, owing to operational challenges stemming from the transient pulsed backpressure of the system, no noticeable improvements in gas quality have been realized to date. Therefore, only preliminary findings for continuous processing are reported herein.

During these runs, the flow reactor was maintained at either a lower thermal state (200 °C) or an elevated temperature range of 400–500 °C. Figure 5 contrasts the resulting dry off-gas compositions obtained via batch loading (squares) and continuous feeding (diamonds) across various feedstock moisture contents (15–70 wt.%). The filled symbols represent a reactor wall temperature of 400–500 °C, whereas the empty symbols correspond to 200 °C. The data indicate that the continuous feeding configuration currently yields a slightly lower-quality gas profile than the baseline batch method, a limitation that is being addressed through ongoing feeder optimization. Regarding thermal

conditioning, elevating the initial reactor temperature consistently promoted CO and H_2 production while mitigating CO_2 dilution, thereby enhancing the overall calorific value of the off-gas.

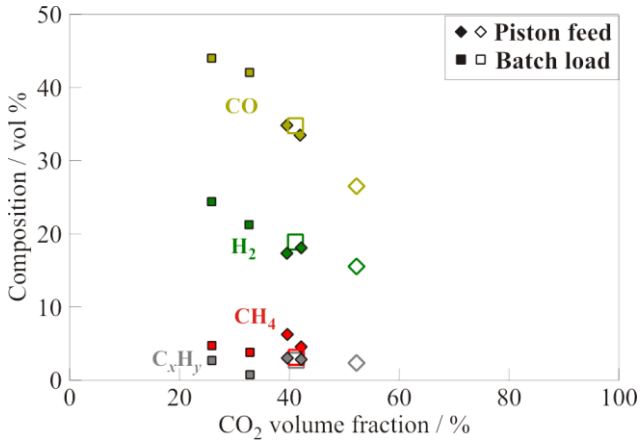

Fig. 5. Measured dependencies of CO, H_2, CH_4, and C_xH_y volume fractions on the volume fraction of CO_2 in the off-gas produced by SM gasification at one-time loading of a weighed feedstock batch (squares) and with gradual feedstock feeding (diamonds) into the flow reactor; the feedstock possesses different moisture contents (from 70% to 15%).

3.8. Effect of feedstock moisture on the yield of solid residue

Experimental measurements indicate that the mass of solid residue recovered from the dry and wet cyclones ranges from 6.7% to 17.8% of the initial dry SM mass when processing raw wet feedstock (α =70%). Reducing the SM moisture content to α =15% causes the solid residue mass to increase to 10%–32.4%, demonstrating that pre-dried SM undergoes more intensive particulate entrainment from the flow reactor than the raw wet biomass, which aligns with expected fluidization and aerodynamic behaviors. To achieve complete conversion within the flow reactor, targeted measures must be implemented to mitigate this premature feedstock carryover. Clearly, the particle residence time inside the reaction zone must be extended, which can be accomplished by integrating intermediate buffer volumes between the PDG and the reactor or by deploying multi-stage cascading reactors.

3.9. Detonability of the off-gas

To characterize the detonability of the dry off-gas, an auxiliary gas accumulation and storage system was integrated into the experimental setup. This system included three wet coalescing filters with replaceable cartridges, a gas compressor with a 50-L tank and a peak capacity of 290 L/min, and a 200-L storage receiver. Pressure within the receiver was monitored via a pressure transducer rated up to 6.0 MPa. Off-gas accumulation experiments were conducted using SM with α = 15%. Composition analysis of the accumulated dry off-gas showed 32% CO_2, 43% CO, 21% H_2, 3% CH_4, and 1% C_xH_y. In the PDG, the stoichiometric mixture of off-gas and oxygen reached a mean detonation velocity of 1800 ± 100 m/s. Although this velocity falls below the measured detonation velocity for a stoichiometric NG–oxygen mixture (2100 ± 100 m/s) because of the lower heating value of the off-gas, its detonability remains adequate. Consequently, replacing NG with this off-gas can potentially support a self-sustaining gasification process.

3.10. Elemental composition and oxidative stability of the solid residue

The elemental composition of the solid residue recovered from the cyclone assembly (following drying) was evaluated for runs #8 and #9. In these trials, the GA mass flow rates were 1.82 g/s and 1.4 g/s, respectively, while the

feedstock configurations were $M_0 = 1000$ g ($\alpha = 70\%$) and 450 g ($\alpha = 15\%$). The residual matrix for run #8 comprised 29.60 wt.% C, 7.50 wt.% O, 1.63 wt.% H, 1.64 wt.% N, and 59.63 wt.% ash, whereas run #9 yielded 42.13 wt.% C, 6.99 wt.% O, 1.98 wt.% H, 2.12 wt.% N, and 46.78 wt.% ash. These profiles demonstrate that the raw wet SM undergoes a deeper thermochemical conversion than the pre-dried feedstock. This behavior is substantiated by: (i) a lower residual carbon fraction in the wet SM char (30 wt.% vs. 42 wt.% for dried SM); (ii) an elevated ash concentration in the wet SM residue (60 wt.% vs. 47 wt.%); and (iii) a threefold reduction in the dry-basis carbon-to-ash ratio for the wet SM compared to the dried matrix. Consequently, the carbon conversion efficiency (CCE) reached 0.99 in run #8, compared to 0.67 in run #9. The near-complete CCE for raw SM is attributed to a gradual, layer-by-layer devolatilization mechanism. Conversely, the suppressed CCE for dried SM stems from rapid particulate entrainment driven by the high fluidizability and lower effective weight of dry particles under the shock-induced GA flow, leading to premature elutriation from the reactor core. Despite this, the lower heating value (LHV) of the off-gas derived from dried SM exceeded that of the wet SM feed. To reconcile these conflicting trends, implementing continuous feedstock injection instead of batchwise loading represents a critical technological requirement.

Figure 6a contrasts the mean mass fractions of various elements in the baseline dried SM with those in the solid residues recovered from the dry and wet cyclones (following condensate drying) across runs #1, #4, and #5. Elemental compositions were quantified via X-ray fluorescence (XRF) using an ARL PERFORM'X spectrometer (Thermo Fisher Scientific Inc., USA). Representative, minor variations in element concentrations between different runs are illustrated in Figure 6b with respect to phosphorus content. The elemental distributions within the dry residues of both cyclones were approximately identical. Given that the aggregate solid residue mass (m_s) in these trials was a factor of 6–7 lower than the initial dry mass (M_d) of the gasified SM batches, the absolute retention of specific elements varied. Notably, the relative concentrations of Ca, P, Al, and Mn in the dry SM were approximately 0.7, 0.5, 0.06, and 0.01 wt.%, respectively, but increased 6–7-fold in the solid residue to roughly 4, 3, 0.4, and 0.07 wt.%. As for Si, Mg, Na, and Cl, their relative contents in the dry SM (1.2, 0.4, 0.2, and 0.1 wt.%, respectively) expanded by only a factor of 2–3 in the solid residue, reaching 3.5, 1.2, 0.4, and 0.2 wt.%. The sulfur concentration remained nearly constant at approximately 0.3 wt.% in both the raw feedstock and the char. This disproportionate concentration effect suggests that elements such as Si, Mg, S, Na, and Cl partially volatilize into the gas phase, bypass the cyclone filtration train, or dissolve into the liquid condensate. The pronounced enrichment of Fe and depletion of V in the solid residue relative to the initial SM matrix warrant further investigation.

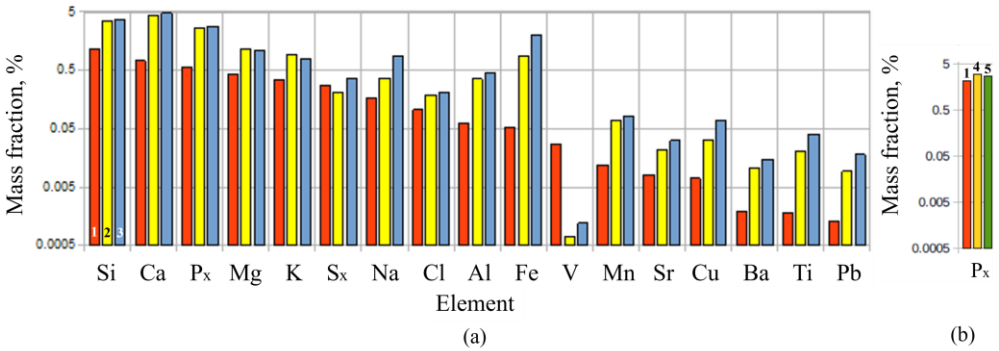

Fig. 6. (a) Mean mass fractions of inorganic elements in the dried feedstock (1, red), dry cyclone solid residue (2, yellow), and wet cyclone solid residue after drying (3, blue); (b) distribution of phosphorus mass fractions in the dry cyclone residue across runs #1, #4, and #5.

The oxidative stability of the solid residue was characterized via simultaneous thermal analysis (DSC/TGA) using an STA ZCT-1 apparatus (JING YI GAO KE, China). Char samples weighing 4.8 mg (sample #1) and 5.2 mg

(sample #2) were placed in ceramic crucibles and heated in an air atmosphere from 50 to 950 °C at a constant heating rate of 10 °C/min. The thermokinetic profiles reveal a single prominent mass loss step, quantified at 36.1% for sample #1 and 52.9% for sample #2. The derivative thermogravimetric (DTG) curves indicate that multiple overlapping degradation pathways of macromolecular segments occurred within the temperature ranges of 317–420 °C and 311–419 °C, respectively, accompanied by distinct caloric effects. The minor variations in the onset temperatures of these decomposition steps are attributed to chemical inhomogeneities between the analyzed samples.

3.11. Granulometric analysis of the solid residue

Figure 7 contrasts the measured particle size distributions (PSDs) of the solid residues recovered from the dry and wet cyclones across runs #2, #5, #6, #8, and #9. The PSDs were quantified via wet laser diffraction using an Analysette 22 apparatus (Fritsch, Germany) in the presence of a surfactant under ultrasonic treatment (50 W). The solid particles exhibit diameters spanning from 0.1 to 35 μm, with the PSD profiles remaining virtually invariant to changes in the experimental conditions.

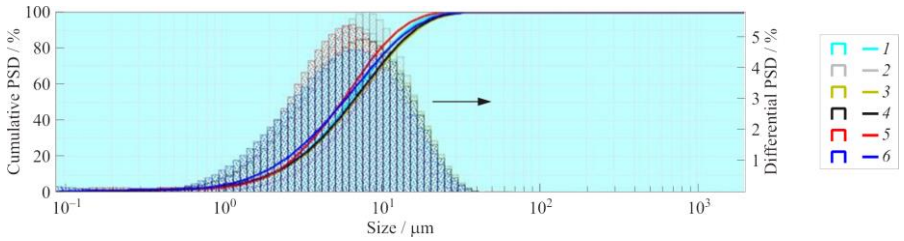

Fig. 7. Particle size distributions of solid residue (1 – experiment #2+#5, 2 – #2; 3 – #5; 4 – #6; 5 – #8; 6 – #9).

3.12. Chemical composition of liquid condensate

Under the baseline batch loading configuration, where an initial period (τ_1, Figure 3a) is dedicated to moisture vaporization, the feedstock simultaneously undergoes low-temperature pyrolytic decomposition promoting the synthesis of various intermediate fractions, including toxic pyrolytic by-products. To evaluate this phenomenon, a qualitative gas chromatography–mass spectrometry (GC-MS) analysis was performed on the liquid constituents recovered from the wet cyclone post-experiment. The analytical protocol and spectroscopic datasets are detailed in Appendix D. The primary identified compounds were phenol and coniferyl alcohol, while species such as toluene, propionic acid, furaldehyde, and furfuryl alcohol were detected in significantly lower concentrations. Following derivatization, the effluent was resolved as trimethylsilyl ethers, revealing an organic matrix rich in acids (propionic, butanoic, valeric, caproic, and benzoic), various furan derivatives, and benzyl alcohol. Thus, to suppress the formation of toxic condensable intermediates, the biomass must be injected continuously into a preheated reactor core. At specific GA mass flow rates and gas residence times, the optimized feedstock supply rate must guarantee the complete conversion of all carbonaceous fractions within the reactor.

4. Discussion

4.1. Mass balances

Data from runs #2, #3, #4, #8, and #12 enabled a precise determination of the mass ratios between the evaporated moisture, gasified dry matter, and supplied GA. Table 2 summarizes the duration of the stage of heating and evaporating feedstock moisture (τ_1); duration of the gasification stage of the dried feedstock (τ_2); total duration of the feedstock gasification process (τ_Σ); initial feedstock batch mass (M_0); moisture content (α); water mass (M_w); dry matter mass (M_d); alongside the mass flow rates of oxygen ($\dot{m}_{ox}$) and NG ($\dot{m}_{fu}$). Furthermore, the data provides the evaluated ratio of total consumed combustible mixture mass to initial feedstock batch mass (M_{fox}/M_0), where $M_{fox} =$

$M_{ox} + M_{fu}$; mass of GA (M_{GA}) consumed for gasification during time interval τ_2; mass of the produced dry off-gas ($M_g = (1-\beta)M_d + M_{GA}$), where β is the ash content in the SM (8.58 wt.%); LHV of the dry off-gas (Q_L, see Table C1); and the dry-basis cold gas efficiency (CGE). The CGE characterizes the potential efficiency of the process for downstream gas utilization. Assuming that high-temperature gasification reactions during time interval τ_2 occur exclusively between the GA and the dry feedstock, a dry-basis CGE estimate can be derived as follows [55]:

$$\mathrm{CGE} = \frac{M_g Q_L}{M_d Q_{L,SM} + M_{GA} H_{GA}} 100\%$$

where $Q_{L,SM}$ corresponds to the LHV of the dry SM (14.6 MJ/kg) and H_{GA} is the specific enthalpy of the GA calculated based on the GA composition at 2000 K (~3,6 MJ/kg).

Table 2 Mass balances of SM drying and gasification processes and dry-basis CGE.

Run #	τ_1 s	τ_2 s	τ_Σ s	M_0 g	α %	M_w g	M_d g	$\dot{m}_{ox}$ g/s	$\dot{m}_{fu}$ g/s	M_{fox}/M_0	M_{GA} g	M_g g	Q_L kJ/g	CGE %
2	300	520	820	1000	70	700	300	1.5	0.33	1.49	950	1220	7.7	121
3	240	600	840	1000	70	700	300	1.5	0.33	1.54	1100	1370	9.6	158
4	160	380	540	1000	70	700	300	2.25	0.53	1.49	1060	1330	7.5	122
8	380	450	830	1000	70	700	300	1.52	0.3	1.52	820	1090	8.8	131
12	260	600	860	1000	45	450	550	1.29	0.27	1.35	940	1440	10.4	131

As indicated by the final M_{fox}/M_0 ratio in Table 2, gasifying 1 kg of wet SM during time interval τ_Σ requires about 1.52 kg and 1.35 kg of GA at moisture contents $\alpha = 70\%$ and 45%, respectively. Linear extrapolation of these data to completely dry SM ($\alpha = 0\%$) yields an experimental SM/GA mass ratio of $\Omega_{exp} \approx 1$, implying a 1:1 mass consumption of GA per unit of dry SM. Mitigating premature feedstock carryover enables the generation of 1.91 kg of combustible off-gas, accounting for a baseline ash content of approximately 9 wt.% in the dry SM. Consequently, the experimental feedstock-to-GA mass ratio was roughly 3.3 times lower than the optimized thermodynamic threshold, establishing a ratio of $\Omega_t/\Omega_{exp} \approx 3.3$.

The evaluated CGE values range between 121% and 158%, thus significantly exceeding the 100% threshold. Under the high-temperature conditions of the PDG, the external thermal energy of the GA is effectively converted into the chemical energy of the resulting H_2- and CO-rich dry off-gas, thereby substantially elevating its cumulative heating value ($M_g Q_L$) relative to the energy content of the dry feedstock ($M_d Q_{L,SM}$) and GA ($M_{GA} H_{GA}$). CGE values exceeding 100% align with findings from several prior studies (e.g., [56], 124%).

To identify the position of the proposed technology among modern waste-to-energy pathways, a formal comparison with mainstream biomass gasification technologies is performed in Table 3. The benchmark includes fluidized bed gasification, plasma gasification, and supercritical water gasification (SCWG), focusing on key performance indicators: CGE, product quality, and economic feasibility, as highlighted in a recent review [57].

Table 3 Comparison of biomass gasification technologies.

Gasification technology	Operating conditions	CGE (%)	Syngas quality	Economic feasibility	Limitations/ Advantages
Fluidized bed	700–900°C, 0.1 MPa	60–80%	Medium; high tar content, cleanup needed	High maturity, low-to-medium CAPEX	Tar formation; fuel flexibility issues

Plasma	>2000°C, 0.1 MPa	50–95%	Excellent; no tar, high H_2/CO ratio	Low, high OPEX/CAPEX	High electricity consumption; scalability issues
SCWG	>374°C, >22.1 MPa	50–100%	High H_2 yield; low tar, high CO_2 fraction	Low due to high pressure equipment	Corrosion, plugging, high equipment costs
PDG	>2000°C 0.1 MPa	120–150%	Excellent; no tar, controlled H_2/CO ratio	High, low OPEX/CAPEX	Explosion safety issues Self-sustaining, Easy scalability

According to Table 3, while fluidized bed gasification represents a commercially mature pathway, its application to complex feedstocks is often hindered by elevated tar yields and the necessity of syngas cleanup to remove toxic compounds and fly ash [58]. Unlike the complex remediation and carbon-recovery strategies required for conventional gasification residues, the proposed PDG technology inherently avoids the formation of such hazardous, complex carbon-ash structures and eliminates the need for extensive post-treatment. Similarly, plasma gasification generates high-quality, virtually tar-free syngas, yet its economic feasibility is compromised by intensive electricity consumption. SCWG serves as an effective route for wet biomass, but demands high operating pressures and its net energy efficiency is often compromised by the high thermal penalty required to maintain supercritical water conditions.

In contrast, the proposed PDG technology offers a more balanced performance profile. Thus, in terms of the CGE, the results obtained in this work are considerably higher than those reported for dual bubbling fluidized bed biomass gasifiers (66% in [59]), values measured (24%–51% in [60]) and estimated (up to 80% in [61]) for steam plasma-assisted gasification, as well as a value of 70% reported in [62] for SCWG. Moreover, the proposed system runs under ambient pressure and features a significantly lower electrical consumption. Power demand is restricted to essential automation and utilities: the control system, a standard automotive spark plug for detonation ignition, and a minor consumption loop for the cooling water pump. It delivers the highest CGE and syngas of controllable quality under milder operating conditions, thereby ensuring a competitive levelized cost of energy. In addition, the PDG system enables self-sustained operation by utilizing its own syngas as fuel, and features straightforward scalability through adjustments to PDG and reactor dimensions as well as PDG operational frequency. Nevertheless, potential constraints regarding explosion safety must be carefully managed. Further aspects, including economic feasibility and safety of the PDG technology, are detailed in [50].

4.2. Energy balances

Runs #8 and #12 were evaluated to characterize the system energy balance. In run #8, a thermal input of 1.84 MJ was theoretically required to heat and vaporize the water within 1 kg of raw feedstock (70% moisture). Chronologically, during the initial drying stage ($\tau_1 = 380$ s) under a PDG frequency of 0.63 Hz, the fuel consumption reached 114 g of NG. This corresponds to an energy input of 5.7 MJ, exceeding the theoretical enthalpy requirement by a factor of approximately 3. Such a discrepancy is attributed to parasitics, specifically heat dissipation into the reactor walls and the coolant of the PDG cooling jackets. Similarly, in run #12 ($\alpha = 45\%$), containing 450 g of water with a theoretical vaporization enthalpy of 1.185 MJ, fuel consumption during the first stage ($\tau_1 = 260$ s) was 72 g of NG. This translates to 3.57 MJ, which also represents a threefold oversupply. Importantly, both trials demonstrate a consistent relative thermal loss to the environment of approximately 67% during the initial stage, independent of the feedstock moisture content. Assuming equivalent heat losses govern the dry-SM conversion phase, it is inferred that only 33% of the GA thermal energy is directly utilized for the physical and chemical transformations of dry SM inside

the flow reactor, while the remaining 67% is dissipated via wall conduction, jacket coolant loops, and sensible heat of the effluent off-gas. Incorporating this real thermal efficiency (33%) into the optimized theoretical feedstock-to-GA mass ratio ($\Omega_t \approx 3.3$, as derived in the modeling section) yields a corrected practical estimate of $\Omega_{exp} \approx 0.33\Omega_t \approx 1$. This value agrees with the experimental mass balance results obtained via the extrapolation of wet SM data ($\Omega_{exp} = 1.52$ at α =70% and $\Omega_{exp} = 1.35$ at α =45% to a zero-moisture baseline.

4.3. Comparison of experimental data with thermodynamic calculations

When comparing the experimental datasets with the thermodynamic equilibrium predictions, several boundary constraints must be factored into the analysis. First, the experimental feedstock moisture ranged from $\alpha = 15\%$ to 70%, whereas a zero-moisture baseline ($\alpha = 0$) was assumed in the calculations. Second, no thermal insulation measures were implemented on the laboratory setup, contrasting with the ideal adiabatic conditions modeled. Third, the measured detonation velocity within the PDG was lower than the theoretical ideal (2100±100 m/s versus 2380 m/s), which altered the initial temperature and composition of the expanded detonation products at 0.1 MPa. Fourth, mixing between the GA and the condensed-phase biomass in the reactor required a finite induction time for particle heating and devolatilization, leading to spatial non-uniformities, whereas instantaneous, molecular-level homogeneous gas-phase mixing was modeled. Finally, contrary to the infinite residence time assumed in the thermodynamic calculations, the real residence time was bounded, allowing for potential kinetic limitations and incomplete conversion.

The combined impacts of feedstock moisture and parasitic heat losses (the first two factors) on process thermal efficiency were quantified in the energy balance section demonstrating that only 33% of the GA thermal energy directly drove the dry-SM phase and chemical transformations, while the remaining 67% was dissipated through wall conduction, cooling jackets, and sensible heat of the effluent off-gas.

Compared to these primary parameters, the influence of the reduced detonation velocity (the third factor) is relatively minor. A velocity deficit of approximately 12% ($|2100 - 2380| \times 100/2380$ =12%) corresponds to a GA temperature drop of less than 20% (from the ideal 2853 K down to ~2280 K, which remains sufficiently high to drive the target chemistry.

The structural consequences of finite mixing rates and spatial non-uniformities are highlighted in Table 4, which contrasts the predicted equilibrium and empirical compositions of the dry off-gas at 1000 K and 0.1 MPa. The final row lists the baseline mole fractions of CO_2, CO, and H_2 within the expanded detonation products exiting the flow reactor in the absence of biomass injection, assuming fully condensed water vapor.

Table 4. Comparison of calculated thermodynamic equilibrium and measured dry off-gas compositions at a gasification temperature of 1000 K and a pressure of 0.1 MPa.

Description	CO_2, vol.%	CO, vol.%	H_2, vol.%	CH_4, vol.%	C_xH_y, vol.%	N_2, vol.%
Calculation ($\alpha = 0$)	10	45	41	-	-	4
Run #7 ($\alpha = 15\%$)	32.7	42.1	21.1	3.6	0.5	-
Run #9 ($\alpha = 15\%$)	32.4	41.4	20	3.6	2.5	-
Run #14 ($\alpha = 15\%$)	42	33.3	17.9	4.3	2.6	-
Run #15 ($\alpha = 15\%$)	39.5	34.6	17.1	6.0	2.9	-
Run #16 ($\alpha = 15\%$)	25.7	44	24.2	4.5	2.5	-
GA	91	6	3	0	0	0

A comparison of the measured CO_2, CO, and H_2 concentrations in the effluent dry off-gas with their baseline values in the GA demonstrates that reactions yielding CO and H_2 proceed actively within the flow reactor, given that

the initial volumetric fractions of these components in the GA were substantially lower. The equilibrium model provides a generally accurate prediction of the CO fraction in the dry off-gas. However, the experimental CO_2 content is a factor of 2–3 higher, whereas the H_2 output is a factor of 2–3 lower than the thermodynamic predictions. Mechanistically, at temperatures exceeding 1200–1300 K, the generation of CO and H_2 is primarily governed by the following reactions:

$$C + H_2O = CO + H_2 \quad \text{(I)}$$

$$C + CO_2 = CO + CO \quad \text{(II)}$$

$$CO + H_2O = CO_2 + H_2 \quad \text{(III)}$$

where C denotes the carbonaceous matrix of the SM. Because the endothermic barrier of reaction (II) exceeds that of reaction (I), and the initial H_2O content in the GA is twofold higher than the CO_2 fraction (65 and 32 vol.%, respectively), the kinetic rate of reaction (II) can be significantly suppressed. This retardation is particularly pronounced at lower localized GA temperatures induced by parasitic heat sinks, specifically moisture vaporization and environmental dissipation. As a result, the input CO_2 constituent within the GA may undergo incomplete thermochemical conversion with the biomass, escaping the reactor vessel within the product stream. This mechanism accounts for the elevated residual CO_2 content observed in the dry off-gas at the terminal equilibrium state of 1000 K. The lower experimental hydrogen output is attributed to substantial spatial non-uniformities governing the heterogeneous pathway of reaction (I).

To shift the actual off-gas composition toward the ideal thermodynamic equilibrium, subsequent engineering efforts must focus on optimizing biomass–GA mixing, elevating the mean internal reactor temperature, and extending the hydrodynamics-driven particle residence time. No fundamental physical limitations hinder the realization of these operational modifications.

5. Conclusions

Experimental studies on the allothermal high-temperature gasification of swine manure were performed across a range of feedstock moisture contents ($\alpha = 15\%$, 45%, and 70%) using a custom laboratory-scale setup. The investigation yielded the following key conclusions:

- **Off-Gas Quality and Biomass Drying:** Gasification of raw wet SM ($\alpha = 70\%$) produced a dry off-gas comprising 33–41 vol.% CO_2, 34–40 vol.% CO, 17–22 vol.% H_2, 2.5–4.0 vol.% CH_4, and 0–2.5 vol.% C_xH_y, achieving a carbon conversion efficiency of 0.99 and the cold gas efficiency ranging between 121% and 158%. Pre-drying the feedstock optimized the gas profiles, elevating the maximum yields of CO, H_2, and CH_4 to 45 vol.%, 25 vol.%, and 5 vol.%, respectively, while decreasing CO_2 to 26 vol.%. This modification increased the total combustible fraction up to 74 vol.%, although the CCE declined to 0.67 due to the premature elutriation of dry biomass particles.
- **Solid Residue Properties:** The particulate matter recovered from the cyclone system exhibited diameters strictly within 0.1–35 μm, whereas the resultant particle size distributions demonstrated negligible sensitivity to variations in the operational parameters.
- **Thermal and Mass Balances:** In the current configuration, 67% of the input thermal energy from the high-temperature detonation products is dissipated via wall conduction, cooling jackets, and sensible off-gas heat, leaving a net thermal efficiency of 33% to drive the gasification chemistry. Under these constraints, the optimal practical feedstock-to-GA mass ratio was established as $\Omega_{\text{exp}} \approx 1$, i.e., processing 1 kg of dry SM requires 1 kg of a stoichiometric NG – O_2 mixture, yielding 1.91 kg of combustible off-gas diluted with 26 vol.% CO_2.

- **Model Validation and Scaling:** The empirical datasets demonstrate parity with thermodynamic equilibrium simulations when factoring in structural heat losses. Transitioning the actual off-gas profiles toward ideal thermodynamic boundaries requires enhancing biomass–GA mixing, increasing the mean reaction zone temperature, and extending the particle residence time. No fundamental physical limitations hinder these system modifications.

Subsequent studies will evaluate the sustainability profile of the developed gasification technology through several key approaches including the reduction of CO_2 concentrations in the off-gas, improving carbon conversion efficiency via continuous feedstock delivery into a preheated reactor core, maximizing the PDG pulse frequency to further accelerate transformation rates and minimize total processing time, and incorporating waste heat recovery systems for internal feedstock preliminary drying.

Appendix A: Measurement techniques

A.1. Gas analysis

The volumetric composition of the generated off-gas was monitored using an MRU Syngas flow-through gas analyzer (Germany), which continuously recorded H_2, CO, CO_2, CH_4, O_2, and N_2 fractions with an estimated measurement error of 5%. Due to the analyzer's lack of selectivity for non-methane hydrocarbons, the cumulative volume fraction of all C_xH_y compounds was inherently co-registered within the N_2 balance. To enhance conditioning and tar removal, the gas stream was routed through a bubbler filled with diesel fuel prior to analyzer injection. For a more detailed characterization of the effluent, including individual C_xH_y species, discrete gas samples were simultaneously extracted for offline analysis on a Chromatec-Crystal 2000 gas chromatograph (Russia). To evaluate the potential trapping or alteration effects of the scrubbing medium on the gas chemistry, sampling ports were positioned both upstream and downstream of the diesel bubbler unit.

A.2. Pressure and temperature measurements

The upper section of the flow reactor was equipped with an overpressure sensor (Kurant DI, Russia; 1% accuracy) and two thermocouples configured to monitor the external reactor wall temperature (Pt100, Russia; accuracy $\pm$1°C) and the local gas temperature (N-type DTPN285, Russia; accuracy $\pm$2.5°C) near the internal wall boundary. The localized gas temperature reading was utilized strictly for stage identification rather than defining the core gasification temperature. The off-gas composition, internal reactor pressure, and upper-zone gas and wall temperatures were continuously recorded throughout each experimental run.

A.3. Analysis of solid residue

Following each experimental run, all solid residues were evacuated from the dual-cyclone system, with the fraction recovered from the wet cyclone subjected to a standard drying procedure. The resulting dry char was subsequently characterized using a comprehensive analytical suite: elemental CHNS analysis via a PE 2400 Series II automatic analyzer (Perkin Elmer, USA; 0.30% abs. accuracy); X-ray fluorescence (XRF) spectrometry on an ARL PERFORM'X instrument (Thermo Fisher Scientific Inc., USA); simultaneous thermal analysis (DSC/TGA) on an STA ZCT-1 apparatus (JING YI GAO KE, China); bomb calorimetry using an ABK-1V system (Russia); and particle size analysis via wet laser diffraction on an Analysette 22 apparatus (Fritsch, Germany) equipped with a 50-W ultrasonic dispersion unit and surfactant addition. The total mass and discrete chemical compositions of the recovered cyclone residues were utilized to quantify the overall feedstock gasification efficiency.

A.4. Analysis of liquid condensate

The H_2O concentration in the produced off-gas was estimated based on the mass of the condensate recovered from the wet cyclone. The chemical composition of this liquid phase was characterized via gas chromatography–mass spectrometry (GC-MS) using a Trace 1310 gas chromatograph coupled with an ISQ mass spectrometric detector (Thermo Fisher Scientific Inc., USA). To extract the organic constituents from the aqueous matrix, a liquid–liquid extraction protocol was performed by adding 4 mL of diethyl ether to a 4-mL condensate sample.

Appendix B: Calorimetric measurements of SM heating values

Table B1 summarizes the bomb calorimetry data for the higher heating value (HHV) of the SM, $Q_{\mathrm{H,SM}}$, obtained using an ABK-1V system (Russia). Due to the high moisture content of the raw feedstock, sample ignition required encapsulation within a 20 μm-thick terylene film pouch secured with a cotton thread. This assembly was placed in the calorimetric bomb crucible, with the thread connected to the ignition wire. The specific heat of combustion of the terylene film was specified as 22,790 J/g. Direct combustion of the SM sample without the auxiliary film was unfeasible due to its elevated moisture content. In Table B1, m_0, m_{f}, m_{i}, m_{w}, and m_{s} denote the masses of the feedstock sample, film, thread, water formed within the bomb crucible, and solid ash residue, respectively, while the higher heating value $Q_{\mathrm{H,SM}}$ is calculated according to the following relation:

$$Q_{\mathrm{H,SM}} = \frac{C \cdot \Delta T - q_{\mathrm{f}} - q_{\mathrm{i}} - q_{\mathrm{ign}}}{m_0}$$

where C represents the heat capacity (energy equivalent) of the calorimeter, ΔT is the corrected temperature rise during the experiment, q_{f} is the combustion enthalpy of the film, q_{i} is the combustion enthalpy of the thread, and q_{ign} is the electrical ignition energy. The mean higher heating value of the initial wet biomass was determined to be approximately 5.8 MJ/kg.

Table B1. Calorimetric data and measured higher heating values (HHV) of the SM samples.

Sample#	m_0^* g	m_{f} g	m_{i} g	m_{w} g	m_{s} g	$\frac{m_{\mathrm{w}}}{m_0} \cdot 100\%$	$Q_{\mathrm{H,SM}}$ MJ/kg
1	2.77380	0.24002	0.00780	2.70	0.14	97	5.64
2	3.08128	0.23941	0.00637	2.97	0.16	96	5.88

*Mass is measured by XP26/M scales (Mettler-Toledo AG, Switzerland) with the accuracy of 10^{-2}mg.

Table B2 presents the transient mass (m) profiles of the SM samples as a function of drying time (t) under ambient room temperature, where the final dry weight is designated as $m_{0\mathrm{d}}$. The kinetic data indicate that mass depletion ceases and stabilizes after approximately 48 hours (two days) of exposure.

Table B2. Transient mass profiles of SM samples as a function of drying time at room temperature.

m, g	77.46	34.59	28.30	28.24
t, hour	0	27	48	52
m/m_{0d}	2.74	1.22	1.002	1

The dried SM sample was combusted in the calorimetric bomb without an auxiliary film. To increase the sample mass and enhance its representativeness, a specialized bomb configuration with two crucibles positioned at different heights within the cavity was utilized. The heat capacity (energy equivalent) of the calorimeter with this modified bomb assembly was calibrated in standalone measurements; it matched the single-crucible configuration once corrected for the discrete heat capacities of the additional crucibles and fittings. The measurement data obtained for the air-dry SM specimens are compiled in Table B3 as runs #1 and #2. Supplementary vacuum drying of the air-dry

sample (pressure $P \leq 0.5$ mm Hg) for 16 hours induced a marginal mass reduction of approximately 0.3 wt.%. The combustion results for this vacuum-dried sample are designated as run #3 in Table B3, where the lower heating value ($Q_{\mathrm{L,SM}}$) is determined via the following expression:

$$Q_{\mathrm{L,SM}} = Q_{\mathrm{H,SM}} - \frac{m_w}{m_0} \cdot 100 \cdot 0.02442 \text{ J/g}$$

Table B3. Experimental calorimetric parameters and net calorific values ($Q_{\mathrm{L,SM}}$) of dried SM.

Sample #	m_0 g	$Q_{\mathrm{H,SM}}$ MJ/kg	m_s g (%)	m_w g (%)	$Q_{\mathrm{L,SM}}$ MJ/kg
1	1.560345	16.53	0.07146 (4.6%)	1.20 (77)	14.6
2	1.615495	16.48	0.074685 (4.6%)	1.24 (77)	14.6
3	1.694625	16.75	0.06724 (4%)	1.20 (71)	15.0

Appendix C: Summary data for some representative experiments

Table C1 Summary data for some representative experiments.

Run #	ν Hz	M_0 g	α %	M_d g	m_s g	$\frac{m_s}{M_d}$,%	τ_1 s	τ_2 s	τ_Σ s	$\dot{m}$ g/s	T_W °C	CO_2 %	CO %	H_2 %	CH_4 %	C_xH_y** %	O_2 %	Q_{Lv} MJ/m^3	Q_L MJ/kg
1	0.78	1500	70	450	80	17.8	300	720	1020	-	260	33.8	38.3	21.7	4.3	1.9	0	10.0	9.5
2	0.63	1000	70	300	50	16.7	300	520	820	-	300	36.1	38.6	21.2	2.8	0.6	0	8.6	7.7
3	0.63	1000	70	300	50	16.7	240	600	840	-	210	33.9	40.4	20.8	3.1	2	0	9.8	9.6
4	1	1000	70	300	49	16.3	160	380	540	-	220	36.5	40.9	19.7	3.5	0	0	8.5	7.5
5*	1	1000	70	300	44	14.7	-	420	420	-	350	40.7	35.1	17.3	3.7	2.4	0	9.3	9.3
6*	1	2000	70	600	72	12.0	-	720	720	-	330	38.5	38.8	18.2	4.1	1.1	0	8.3	7.3
7	0.77	800	15	680	220	32.4	130	1200	1330	-	320	32.7	42.1	21.1	3.6	0.5	0	9.2	8.3
8	0.63	1000	70	300	20	6.7	380	450	830	-	150	41.3	34.7	18.7	2.5	2.2	0	8.8	8.8
9*	0.50	450	15	425	80	20.9	290	300	590	-	230	32.4	41.4	20	3.6	2.5	0	10.3	10.4
10	0.63	1000	70	300	30	10.0	-	660	660	-	220	38.7	37	18.7	3.5	1.9	0.3	8.9	9.7
11	0.77	1000	45	550	90	16.4	-	600	600	-	250	34.7	39.3	19.4	4	2.5	0.2	9.7	10.5
12	0.63	1000	45	550	90	16.4	260	600	860	-	240	34	39.6	20.6	3.7	1.9	0.3	9.5	10.4
13*	0.63	2000	70	600	-	-	-	600	600	3.3	170	52.2	26.4	15.3	2.1	2.1	2.1	6.8	7.4
14*	0.63	650	15	617.5	66	10.7	-	980	980	0.62	460	42	33.3	17.9	4.3	2.6	0	9.0	9.8
15	0.63	650	15	617.5	62	10	-	1000	1000	0.62	390	39.5	34.6	17.1	6	2.9	0	9.8	10.8
16	0.63	500	15	475	134	28.2	-	280	280	-	400	25.7	44	24.2	4.5	2.5	0	11.0	12.1
17	0.63	500	70	150	20	13.3	-	260	260	-	370	39.3	35.5	18.4	3.8	2.6	0	9.1	9.9

* Preheating of the reactor; **The heat of combustion for C_xH_y is taken equal 70 MJ/m^3, density 1.6 kg/m^3;

ν is the operation frequency of the PDG; M_0 is the mass of the original (wet) feedstock; α is the moisture content in the feedstock; M_d is the mass of dry matter in the feedstock; m_s is the mass of the solid residue after gasification; τ_1 is the duration of the stage of heating and evaporating feedstock moisture; τ_2 is the duration of the gasification stage of the dried feedstock; τ_Σ is the total duration of the feedstock gasification process; $\dot{m}$ is the mass flow rate of feedstock when supplied continuously from the feeder; and T_W is the temperature of the reactor wall. In addition, the table shows the measured composition of the dry off-gas in terms of CO_2, CO, H_2, CH_4, C_xH_y, and O_2 volume fractions as well as volumetric Q_{Lv} and mass Q_L lower heating values of the dry off-gas.

Appendix D: Composition of liquid condensate

Liquid condensate was characterized using a Trace 1310 gas chromatograph coupled with an ISQ mass spectrometric detector (Thermo Fisher Scientific, USA). Chromatographic separation was achieved on a TR-5MS fused-silica capillary column (15 m × 0.32 mm ID, 0.25 μm film thickness) with a 5% phenyl–95% methylpolysiloxane stationary phase. The oven temperature program was initiated at 40 °C (held for 3 min), ramped to 120 °C at 5 °C/min, further accelerated to 300 °C at 15 °C/min, and finally held at 300 °C for 5 min. The injector temperature was maintained at 220 °C. Samples (1 μL) were injected utilizing a split operating mode (split ratio 1:40). Mass spectra were acquired via electron ionization (EI) at 70 eV over a scanning range of 35–600 amu with a scan speed of 0.3 scan/s.

Liquid–liquid extraction was executed by adding 4 mL of diethyl ether to a 4-mL condensate aliquot. The mixture was continuously agitated for 10 min to ensure uniform mass transfer. Following phase separation, the upper organic layer was collected and dehydrated by filtration through a layer of anhydrous sodium sulfate over a paper filter. This extraction protocol was repeated twice using fresh solvent. The combined ether extracts were subsequently concentrated to a residual volume of 1–2 mL via rotary evaporation under vacuum at room temperature.

Silylation derivatization was performed using N,O-bis(trimethylsilyl)trifluoroacetamide (BSTFA) as the silylating agent. Initially, a 200-μL aliquot of the concentrated ether extract was evaporated to absolute dryness at 50 °C. The dry residue was treated with 20 μL of BSTFA and silylated at 50 °C for 15 min. The mixture was then reconstituted in 200 μL of hexane and analyzed via the aforementioned GC-MS protocol. Figure 8 illustrates the total ion current (TIC) chromatograms of the crude diethyl ether extract (Figure 8a) and the hexane extract containing the trimethylsilyl derivatives of the SM thermochemical conversion products (Figure 8b).

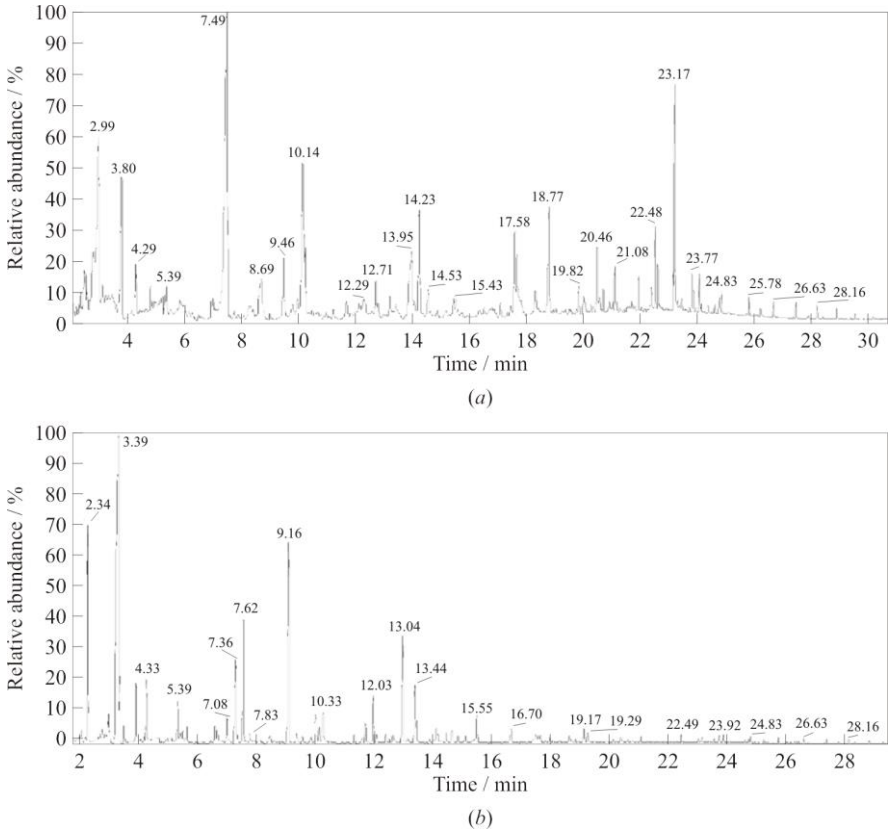

Fig. 8. Total ion current chromatograms of (a) the crude diethyl ether extract and (b) the hexane extract containing trimethylsilyl derivatives from the SM gasification product condensate.

The following pyrolysis/gasification products were identified in the sample:

- Main compounds (the most intense peaks on the chromatogram): phenol (emission time 7.49 min) and coniferyl alcohol (23.17 min);

- Major compounds: toluene (1.77 min), propionic acid (1.96 min), furaldehyde (2.99 min), furfuryl alcohol (3.80 min), dimethylbenzene isomer (4.29 min), methyl phenol isomers (9.46 min and 10.14 min), dihydroxy benzene isomer (13.95 min), coumaran (14.23 min), syringol (17.58 min), vanillin (18.77 min), acetovanillone (20.46 min), syringyl aldehyde (22.48 min), dihydroxymethylguaiacol (22.58 min);

- Minor compounds: ethylphenol isomers (12.71 min and 12.78 min), methylguaiacol (13.20 min), hydroxybenzaldehyde isomer (18.29 min), acetosyringol (23.12 min).

Compounds characteristic of lignin pyrolysis products were identified in the SM pyrolysis/gasification products: methylguaiacol, syringol, acetovanillone, vanillin, and others. It can be assumed that the SM pyrolysis/gasification products also contain other compounds typical of lignin pyrolysis products: various acids and alcohols, which were not detected because the stationary phase of the TR-5MS capillary column used in GC-MS analysis was weakly polar and was not suitable for analyzing such highly polar compounds as alcohols and acids, especially linear and low-molecular ones.

After derivatization, the following products were identified as trimethylsilyl ethers (Figure 8b):

- Acids: C5 oxyacid with a molecular weight of 116 (2.15 min), propionic acid (2.34 min), methylpropionic acid (3.04 min), butanoic acid (4.33 min), methylbutanoic acid isomers (4.76 min and 5.71 min), valeric acid (7.08 min), C6 acid with a molecular weight of 116 (7.83 min), caproic acid (9.92 min), benzoic acid (14.71 min), hydrocinnamic acid (19.17 min);

- Furan derivatives: furfuryl alcohol (7.62 min), coumaran (14.18 min). Phenols: phenol (9.16 min), methylphenol isomer (11.39 min, 11.75 min and 12.03 min), dihydroxybenzene monoester isomer (13.44 min), guaiacol (14.22 min), ethylphenol isomer (14.49 min), dihydroxybenzene diester isomer (16.70 min), hydroxybenzaldehyde (18.00 min), dimethoxyphenol (18.88 min), hydroxyacetophenone (20.16 min), vanillin (21.11 min);

- Alcohols: benzyl alcohol (12.14 min).

Analysis and identification of silyl derivatives also showed that the pyrolysis/gasification products of SM are similar to the pyrolysis products of lignin.

Abbreviations

CCE Carbon conversion efficiency
CJ Chapman – Jouguet
EC Electrical conductivity
GA Gasifying agent
IP Ionization probe
IR Infra-red
NG Natural gas
PDG Pulsed detonation gun
PSD Particle size distribution
SCWG Supercritical water gasification
SM Swine manure
HHV higher heating value
LHV lower heating value

CGE cold gas efficiency

XRF X-ray fluorescence

GC-MS gas chromatography–mass spectrometry

DSC Differential Scanning Calorimetry

TGA Thermogravimetric Analysis

DTG derivative thermogravimetric

BSTFA N,O-bis(trimethylsilyl)trifluoroacetamide

Nomenclature

C	heat equivalent of the calorimeter
c_p	specific heat capacity of water
M_0	mass of the original (wet) feedstock
M_{CJ}	Mach number of Chapman – Jouguet detonation
M_{GA}	mass of GA consumed for gasification during time interval τ_2
M_{d}	mass of dry matter in the feedstock
M_{fox}	mass of consumed combustible mixture
M_{fu}	mass of consumed NG
M_{g}	mass of the produced off-gas
M_{w}	mass of water in a feedstock batch
m	mass of SM sample at time t
m_0	mass of original wet SM sample
$m_{0\mathrm{d}}$	mass of dry SM sample
m_{f}	mass of film
$\mathrm{m_i}$	mass of thread
m_{s}	mass of the solid residue in the crucible
m_{w}	mass of water formed in the bomb crucible
$\dot{m}$	mass flow rate of feedstock when supplied continuously from the feeder
$\dot{m}_{\mathrm{f}}$	heat of combustion of the film
$\dot{m}_{\mathrm{fu}}$	mass flow rate of fuel
Q_{ev}	latent heat of water evaporation
Q_{H}	off-gas higher heating value per unit mass
$Q_{\mathrm{H,SM}}$	feedstock higher heating value per unit mass
Q_L	off-gas lower heating value per unit mass
$Q_{\mathrm{L,SM}}$	feedstock lower heating value per unit mass
Q_{Lv}	off-gas lower heating value per unit volume
P_0	initial pressure
q_{i}	heat of combustion of the thread
q_{ign}	ignition energy
q_{ox}	mass flow rate of oxygen
T_{G}	mean gas temperature
T_{W}	reactor wall temperature
t	time
α	moisture content in feedstock
β	ash content
ΔT	temperature rise in experiment
ΔT_{w}	the difference between water boiling temperature and the initial temperature of wet feedstock
ν	operation frequency of PDG
τ_1	time interval of water evaporation stage
τ_2	time interval of gasification stage of the dried feedstock
τ_Σ	total duration of gasification process
Φ	fuel–to–oxygen equivalence ratio
Ω_{exp}	experimental SM/GA mass ratio
Ω_{t}	optimal theoretical SM/GA mass ratio

Author Contributions: Conceptualization, S.M.F.; methodology, S.M.F. and V.A.S.; software, K.A.A.; formal analysis, S.M.F., V.A.S., I.A.S., and A.S.S.; validation, A.S.S, I.A.S., and V.A.S. investigation, V.A.S., I.A.S., A.S.S.;

visualization, I.A.S., and V.A.S.; resources, S.M.F.; data curation, F.S.F. and A.S.S.; writing—original draft preparation, S.M.F. and V.A.S.; writing—review and editing, S.M.F.; supervision, S.M.F.; project administration, S.M.F. All authors have read and agreed to the published version of the manuscript.

Funding

This research received no external funding.

Availability of Data and Material

The data will be available on request.

Conflicts of interest

The authors declare no conflicts of interest.

Acknowledgments

The authors are grateful to Aleksey B. Vorobyov, Aleksey V. Inozemtsev, Yaroslav O. Inozemtsev, Elena V. Koverzanova, Yurii A. Gordienko, Tatiana V. Dudareva, and Vera Ya. Popkova from the Semenov Federal Research Center for Chemical Physics, 4 Kosygin Str., 119991 Moscow, Russia, and Nikolai D. Blinov from the Federal Scientific Agroengineering Center VIM, 5, 1st Institutsky Proezd, 109428 Moscow, Russia, for their valuable assistance with measuring the physicochemical properties of the feedstock.

References

1. Ndue, K., Pál, G. 2022. Life cycle assessment perspective for sectoral adaptation to climate change: Environmental impact assessment of pig production, Land 11, 827, https://doi.org/10.3390/ land11060827.
2. Cruz, P., Menon, S., and Rice, C. 2026. Sustainable swine production: reducing environmental impacts through cropping systems and manure management, J Animal Sci. 104, skaf428, https://doi.org/10.1093/jas/skaf428.
3. Merzlaya, G.E., Shchegoleva, I.V., and Leonov, M.V. 2012. Use of pig manure for fertilizing agricultural crops. Prosp. Pig Breeding: Theory Pract. 6, 3-9.
4. Zhang, S., Du, M., Ge, H., Rong, S., Chen, Y., Guo, L., 2024. Sulfur migration mechanism of pig manure in supercritical water: A combined experimental and DFT study, J Hazard Mater 471, 134376, https://doi.org/10.1016/j.jhazmat.2024.134376.
5. Shalavina, E.V., Bryukhanov, A.Yu., Vasiliev, E.V., Uvarov, R.A., and Valge, A.M. 2020. Biofermentation of organic waste from a pig-breeding complex in a drum-type installation. Agricult. Sci. 339(6), 51–56.
6. Wang, D, Lin, J.Y., Sayre, J.M., Schmidt, R., Fonte, S.J., Rodrigues, J.L.M., and Scow, K.M., 2022. Compost amendment maintains soil structure and carbon storage by increasing available carbon and microbial biomass in agricultural soil – A six-year field study, Geoderma 427, 116117, https://doi.org/10.1016/j.geoderma.2022.116117.
7. Li, S., Zou, D., Li, L., Wu, L., Liu, F., Zeng, X., Wang, H., Zhu, Y., and Xiao, Z. 2020.Evolution of heavy metals during thermal treatment of manure: a critical review and outlooks. Chemosphere 247, 125962.
8. Hei, Z., Peng, Y., Hao, S., Li, Y., Yang, X., Zhu, T., Müller, C., Zhang, H., Hu, H., and Chen, Y., 2023. Full substitution of chemical fertilizer by organic manure decreases soil N2O emissions driven by ammonia oxidizers and gross nitrogen transformations. Glob. Change Biology 29, 7117–7130. https://doi.org/10.1111/gcb.16957.
9. Gaur, V.K., Sharma, P., Sirohi, R., Awasthi, M.K., Dussap, C.-G., Pandey, A., 2020. Assessing the impact of industrial waste on environment and mitigation strategies: A comprehensive review, J Hazard Mater 398, 123019, https://doi.org/10.1016/j.jhazmat.2020.123019.
10. Liang, Y. 2021. A critical review of challenges faced by converting food waste to bioenergy through anaerobic digestion and hydrothermal liquefaction. Waste Biomass Valoriz. 1–16.

11. Gaifullin, I.Kh., Ziganshin, B.G., Shornikov, A.V., Ivanov, B.L., and Zinnatullina, A.N. 2024. Theoretical aspects of the process of biogas production during anaerobic fermentation of organic waste. Eng. Techn. Animal Husbandry 14(1), 90-95. DOI 10.22314/27132064-2024-1-90.
12. Fernandez-Lopez, M., Pedrosa-Castro, G.J., Valverde, J.L., Sanchez-Silva, L., 2016. Kinetic analysis of manure pyrolysis and combustion processes, Waste Management 58, 230–240, http://dx.doi.org/10.1016/j.wasman.2016.08.027.
13. Shen, C.; Zhang, Y.; Liu, G.; Wang, D.; Zhang, J.; Yang, K.; Wen, X.; Sun, Q.; Dou, X.; Zhang, Y.; Mao, J.; Deng, L., 2025. Thermogravimetric analysis of blended fuel of pig manure, straw, and coal. Energies 18, 3447, https://doi.org/10.3390/ en18133447.
14. Domingos, Y., Abad, A., De Las Obras Loscertales, M., Izquierdo, M.T., Cabello, A., 2025. Chemical looping combustion and gasification of swine manure with a Cu-Based oxygen carrier, Chem. Eng. J. 503, 158503, https://doi.org/10.1016/j.cej.2024.158503.
15. Shen, C., Zhang, Y., Liu, G., Wang, D., Zhang, J., Yang, K., Wen, X., Sun, Q., Dou, X., Zhang, Y., Mao, J., and Deng, L., 2025. Thermogravimetric analysis of blended fuel of pig manure, straw, and coal, Energies 18, 3447. https://doi.org/10.3390/ en18133447.
16. Ro, K., Libra, J., Bae, S., Berge, N., Flora, J., and Pecenka, R. 2019. Combustion behavior of animal-manure-based hydrochar and pyrochar. ACS Sustain. Chem. Eng. 7, 470–478.
17. Szulc, W., Rutkowska, B., Gawroński, S., and Wszelaczyńska, E. 2021. Possibilities of using organic waste after biological and physical processing—an overview. Processes 9(9), 1501.
18. He, L., Wang, D., Zhu, T., Lv, Y., and Li, S., 2023. Pyrolysis recycling of pig manure biochar adsorption material for decreasing ammonia nitrogen in biogas slurry, Sci. Total Environment 881, 163315, https://doi.org/10.1016/j.scitotenv.2023.163315.
19. Zhao, F., Li, D., Chen, H., Zeng, X., Lin, L., Yuan, H., Shan, R., Chen, Y., 2025. Pyrolysis of pig waste from intensive farming operations: Kinetics, product distribution, and transformation of endogenous heavy metals, J Hazard Mater 491, 137916, https://doi.org/10.1016/j.jhazmat.2025.137916.
20. Wu, Q., Huang, S., Li, Q., Zheng, X., Liu, W., Zhu, R., Tang, J., Dai, B., Mo, Y., Zhan, L., Xiong, J., Xiao, Z., 2026. Catalytic liquefaction of pig manure in ethanol: Yield and properties of bio-oil, Biomass and Bioenergy 207, 108796, https://doi.org/10.1016/j.biombioe.2025.108796.
21. Zhou, C.-F., Zhou, C.-H., Liu, X.-P., Jiang, M., Lu, H.-C., Mei, K.-J., Wu, Y.-Q., Wang, G.-F., Li, L., Yin, X., Huang, Y.-J., Huang, H.-J., 2026. Enhancement of the hydrothermal carbonization of pig manure using bio-based surfactants: Product distribution and characteristics, pollutant control, and preliminary mechanisms, J. Analyt. Appl. Pyrolysis 193, Part 1, 107394, https://doi.org/10.1016/j.jaap.2025.107394.
22. Spiridonova, A.V., Druzyanova, V.P., Osmonov, O.M., Tarabukina, O.K., and Sivtseva, Zh.G. 2022. Pyrolysis technology is a promising method for utilizing solid dried manure. Far East. Agrar. Bull. 1(61), 143–150. Doi: 10.24412/1999-6837-2022-1-143-150.
23. Su, G., Ong, H.C., and Mohd Zulkifli, N.W. 2022. Valorization of animal manure via pyrolysis for bioenergy: a review. J. Clean Prod. 343, 130965. https://doi.org/10.1016/j.jclepro.2022.130965.
24. Zhang, S., Huang, F., Morishita, K., and Takarada, T. 2009. Hydrogen production from manure by low temperature gasification. 2009 Asia-Pacific Power and Energy Engineering Conference. doi:10.1109/appeec.2009.4918410.
25. Basu, P. *Biomass Gasification and Pyrolysis: Practical Design and Theory.* Academic Press, New York, 2010.
26. Lombardi, L., Carnevale, E., and Corti, A. 2015. A review of technologies and performances of thermal treatment systems for energy recovery from waste. Waste Manag. 37, 26–44.
27. McKendry, P. 2002. Energy production from biomass (part 3): gasification technologies. Bioresour. Technol. 83(1), 55–63.
28. Vamvuka, D., Sfakiotakis, S., and Pantelaki, O. 2019. Evaluation of gaseous and solid products from the pyrolysis of waste biomass blends for energetic and environmental applications. Fuel 236, 574–582.
29. Naranjo Herrera, A.M., Mano Esteves, E.M., Mansouri, M., Breuhaus, P., Vaz Morgado, C.R., 2026. Brazilian bioenergy generation from cattle and pig manure: An economic life cycle assessment, Renewable Energy 262, 125345, https://doi.org/10.1016/j.renene.2026.125345.

30. Pu, M.; Zhang, Y.; Mukherjee, S.; Alharbi, S.F.; Singh, R.K.; Abou-Elwafa, S.F.; Trindade, H.; Zhang, T., 2025. Impact of combined application of swine manure liquid and phosphorus fertilizers on soil phosphorus and microbial communities, Sustainability17, 2037, https://doi.org/10.3390/ su17052037.
31. Zhang, X., Mao, X., Pi, L., Wu, T., and Hu, Y. 2019. Adsorptive and capacitive properties of the activated carbons derived from pig manure residues. J. Environ. Chem. Eng. 7, 103066.
32. Park, M.H., Kumar, S., and Ra, C. 2012. Solid waste from swine wastewater as a fuel source for heat production. Asian-Aust. J. Anim. Sci. 25, 1627–1633.
33. Wu, H., Hanna, M.A., and Jones, D.D. 2013. Life cycle assessment of greenhouse gas emissions of feedlot manure management practices: Land application versus gasification. Biomass Bioenergy 54, 260–266.
34. Mohan, D., Pittman, C.U., and Steele, P.H. 2006. Pyrolysis of wood/biomass for bio-oil: A critical review. Energy Fuels 20, 848–889.
35. He, B.J., Zhang, Y., Yin, Y., Funk, T.L., and Riskowski, G. 2001. Preliminary characterization of raw oil products from the thermochemical conversion of swine manure. Trans. ASAE 44, 1865–1871.
36. Mullen, C.A. and Boateng, A.A. 2008. Chemical composition of bio-oils produced by fast pyrolysis of two energy crops. Energy Fuels 22, 2104–2109.
37. Azuara, M., Kersten, S.R., and Kootstra, A.M.J. 2013. Recycling phosphorus by fast pyrolysis of pig manure: concentration and extraction of phosphorus combined with the formation of value-added pyrolysis products. Biomass Bioenergy 49, 171–180.
38. Cao, J., Xiao, X., Zhang, S., Zhao, X., Sato, K., Ogawa, Y., Wei, X.Y., and Takarada, T. 2011. Preparation and characterization of bio-oils from internally circulating fluidized-bed pyrolyses of municipal, livestock, and wood waste. Bioresour. Technol. 102, 2009–2015.
39. Elliott, D.C. 2007. Historical developments in hydroprocessing bio-oils. Energy Fuels 21, 1792–1815.
40. Cantrell, K.B., Hunt, P.G., Uchimiya, M., Novak, J.M., and Ro, K.S. 2012. Impact of pyrolysis temperature and manure source on physicochemical characteristics of biochar. Bioresour. Technol. 107, 419–428.
41. Takanabe, K., Aika, K., Seshan, K., and Lefferts, L. 2004. Sustainable hydrogen from bio-oil—Steam reforming of acetic acid as a model oxygenate. J. Catal. 227, 101–108.
42. Burra, K.G., Hussein, M.S., Amano, R.S., and Gupta, A.K. 2016. Syngas evolutionary behavior during chicken manure pyrolysis and air gasification. Appl. Energy 181(1), 408–415.
43. Maric, J., Berdugo Vilches, T., Pissot, S., Cañete Vela, I., Gyllenhammar, M., and Seemann, M. 2020. Emissions of dioxins and furans during steam gasification of Automotive Shredder residue; experiences from the Chalmers 2–4-MW indirect gasifier. Waste Manag. 102, 114–121. https://doi.org/10.1016/j.wasman.2019.10.037
44. Frolov, S.M. Organic waste gasification: A selective review. 2021. Fuels 2, 556–651. DOI: 10.3390/fuels2040033.
45. Messerle, V.E., Ustimenko, A.B., Lavrichshev, O.A., and Nugman, M.K. 2024. The gasification and pyrolysis of biomass using a plasma system. Energies 17, 5594. https:// doi.org/10.3390/en17225594.
46. Rosyadi, I., Suyitno, S., Ilyas, A.X., Faishal, A., Budiono, A., and Yusuf, M. 2022. Producing hydrogen-rich syngas via microwave heating and co-gasification: a systematic review. Biofuel Res. J. 33, 1573-1591. DOI: 10.18331/BRJ2022.9.1.4.
47. Frolov, S.M., Smetanyuk, V.A., Avdeev, K.A., and Nabatnikov, S.A. Method for obtaining highly overheated steam and detonation steam generator device (options). Patent of Russian Federation No. 2686138 dated 24.04.2019.
48. Frolov, S.M., Silantiev, A.S., Sadykov, I.A., Smetanyuk, V.A., Frolov, F.S., Hasiak, J.K., Dudareva, T.V., Bekeshev, V.G., Grishin, M.V., Golubev, E.K., Baimukhambetova, D., Popkova, V.Y., Vezentsev, A.I., Razdobarin, A.E., Yapryntsev, M.N., and Sokolovskiy, P.V. 2023.Composition and textural characteristics of char powders produced by thermomechanical processing of sunflower seed husks. Powders 2, 624–638. https://doi.org/10.3390/powders2030039.
49. Frolov, S.M., Silantiev, A.S., Sadykov, I.A., Smetanyuk, V.A., Frolov, F.S., Hasiak, J.K., Vorob'ev, A.B., Inozemtsev, A.V., and Inozemtsev, J.O. 2023. Gasification of waste machine oil by the ultra-superheated mixture of steam and carbon dioxide. Waste 1, 515–531. https://doi.org/ 10.3390/waste1020031.
50. Frolov, S.M. 2023. Organic waste gasification by ultra-superheated steam. Energies 16, 219. https://doi.org/10.3390/en16010219.

51. Frolov, S.M., Smetanyuk, V.A., Sadykov, I.A., Silantiev, A.S., Frolov, F.S., Popkova, V.Y., Hasiak, J.K., Buyanovskaya, A.G., Takazova, R.U., Dudareva, T.V., Bekeshev, V.G., Vorobyov, A.B., Inozemtsev, A.V., and Inozemtsev, J.O. 2025. High-temperature steam- and CO2-assisted gasification of oil sludge and petcoke. Clean Technologies 7, 17. https://doi.org/10.3390/cleantechnol7010017.
52. Avdeev, K.A., Silantiev, A.S., Smetanyuk, V.A., Piletsky, V.G., Frolov, F.S., and Frolov, S.M. 2024. Conditions for self-feeding of pulsed detonation guns with energy gas during gasification of brown coals by detonation products. Gorenie Vzryv 17(1), 95–104. DOI: 10.30826/CE24170108.
53. SDToolBox – Numerical tools for shock and detonation wave modeling. https://shepherd.caltechedu/SDT (accessed on March 13, 2025).
54. Goodwin, D.G., Moffat, H.K., Schoegl, I., Speth, R.L., and Weber, B.W. *Cantera: An object-oriented software toolkit for chemical kinetics, thermodynamics, and transport processes*. https://www.cantera.org, 2023. Version 3.0.0. doi:10.5281/zenodo.8137090 (accessed on March 13, 2025).
55. Tavakoli, N., Saidi, M., 2024. Exergy analysis and cold gas efficiency evaluation for hydrogen generation through algae biomass steam gasification coupled with water-gas shift reaction, Int. J. Hydrogen Energy 57, 500-514, https://doi.org/10.1016/j.ijhydene.2023.11.323.
56. Dascomb, J., Krothapalli, A., Fakhrai, R., 2013. Thermal conversion efficiency of producing hydrogen enriched syngas from biomass steam gasification, Int. J. Hydrogen Energy 38(27), 11790-11798, https://doi.org/10.1016/j.ijhydene.2013.07.022.
57. Nicolucci, E., Palone, O., Wu, S., Xiao, R., Markides, C.N., Borello, D. From waste to wealth: Can fluidized-bed gasification transform industrial practices? Applied Thermal Engineering 2026, **286**. 129246.
58. Cheng, G., Guo, R., Gao, P., Xu, C., Duan, P., Zhang, Z., Deng, X., Yan, K., Cheng, F., 2026. Research on surface hydrophobic modification and flotation decarbonization of coal gasification fine slag, Chem. Eng. J., 529. 172241, https://doi.org/10.1016/j.cej.2025.172241.
59. Di Carlo, A.; Savuto, E.; Foscolo, P.U.; Papa, A.A.; Tacconi, A.; Del Zotto, L.; Aydin, B.; Bocci, E., 2022. Preliminary results of biomass gasification obtained at pilot scale with an innovative 100 kWth dual bubbling fluidized bed gasifier. Energies 15, 4369.
60. Diaz, G. Sharma, N., Leal-Quiros, E., Munoz-Hernandez, A., 2015. Enhanced hydrogen production using steam plasma processing of biomass: Experimental apparatus and procedure, Int. J. Hydrogen Energy 40(5), 2091-2098, https://doi.org/10.1016/j.ijhydene.2014.12.049.
61. Bastek, S., Dossow, M., Tamošiūnas, A., Umeki, K., Spliethoff, H., Fendt, S., 2025. Technical evaluation of plasma-assisted entrained flow gasification for hydrogen-rich syngas production from waste and biomass, Int. J. Hydrogen Energy 157, 150184, https://doi.org/10.1016/j.ijhydene.2025.150184.
62. Yakaboylu, O., Harinck, J., Smit, K.G., De Jong, W., 2015. Supercritical water gasification of biomass: A literature and technology overview, Energies 8, 859-894, https://doi.org/10.3390/en8020859.